International Journal of Mathematical, Engineering and Management Sciences
Vol. 10, No. 1, 129-147, 2025
https://doi.org/10.33889/IJMEMS.2025.10.1.008

Development of Improved Superconducting Pulsed Power Supply using Three-Winding Pulsed Power Transformer with Energy Recovery

Ayaz Ahmed
Institute of High Voltage & High Current,
Universiti Teknologi Malaysia, Johar Bahru, Malaysia.
E-mail: ayaz@graduate.utm.my

Zulkurnain Abdul-Malek
Institute of High Voltage & High Current,
Universiti Teknologi Malaysia, Johar Bahru, Malaysia.
E-mail: zulkurnain@utm.my

Hasmat Malik
Department of Electrical Power Engineering,
Faculty of Electrical Engineering, Universiti Teknologi Malaysia (UTM), Johor Bahru, 81310, Malaysia.
&
Department of Electrical Engineering,
Graphic Era Deemed to be University, Dehradun, Uttarakhand, India.
E-mail: hasmat@utm.my

Tariq Ali Chandio
School of Chemical and Energy Engineering,
Universiti Teknologi Malaysia, Johar Bahru, Malaysia.
E-mail: tariqalichandio@graduate.utm.my

(Received on December 26, 2023; Revised on April 9, 2024 & July 10, 2024 & July 27, 2024 & September 27, 2024; Accepted on October 10, 2024)

Abstract
The advantages of superconducting pulsed power supplies (SPPS)-such as higher energy density, extended storage time, low losses, and fewer power requirements for power source charging-have increased in popularity. A prior study presented an improved SPPS capable of energy recovery by adjusting two capacitors in a switching circuit to promote residual energy recovery. However, there are still unresolved issues; while the energy recovery can be improved further, the output peak current cannot attain higher levels. This article discusses the implementation of a three-winding pulse transformer (TWPT) to increase the load current and two capacitors in the switching circuit to improve the recovery of residual energy at a consistent rate. The single secondary winding of the TWPT is made of copper, whereas the two main windings are composed of superconducting tape. Theoretical and simulation modelling demonstrates that the load current increases by 29% and the total energy recovery increases by 2.9% at a constant 25 Hz operating frequency.

Keywords- Superconducting pulsed power supply, Inductive pulsed power supply, Energy recovery, Operating frequency, Repetitive pulse current.

1. Introduction

A pulse power supply is a device that releases electrical energy to the load in the form of a single or several rapid pulses with variable repetition frequency. Batteries, capacitors, and inductors are some examples of energy storage devices, while the use of capacitors as energy storage devices in pulse power supplies is widespread (Mcnab, 2001). However, with the advancement of superconducting materials, researchers are more interested in the development of inductive pulse power supplies (IPPSs) because they have higher energy densities than capacitive ones (Liebfried, 2017; Sitzman et al., 2007). Compared with the capacitive one, the IPPS has higher energy density with low losses (Bluhm, 2006). In an IPPS, an energy-storing inductor may be a superconducting coil or a regular conducting coil.

IPPS is mainly based on three topological circuits, XRAM ("MARX" backward spelling), meatgrinder, and the pulse transformer. The XRAM current multiplier circuit is a well-known technique for producing high-current pulses. In terms of impression, it is like the more widely recognised voltage multiplier "MARX". The MARX circuit generates high-voltage pulses by charging capacitors in parallel, then switching them to discharge in series (Bae et al., 2010). Different XRAM based circuits have been derived in the literature (Dedié et al., 2011a; Dedié et al., 2011b; Kanter et al., 1993; Ma et al., 2017; Zhao et al., 2020), the second IPPS topology is meatgrinder. In this topology, different inductors are serially charged and all inductors are discharged to the last inductor by switches (Lindner et al., 1986). The literature has proposed various derivative circuits over time (Liu and Yu, 2017; Sitzman et al., 2005; Sun et al., 2020; Yu et al., 2017; Yu and Chu, 2013).

IPPS using superconducting coils, normally known as superconducting pulsed power supplies (SPPS), have more advantages over normal coils like higher energy density, very low resistance losses, and higher time of energy storage. These benefits have drawn a lot of researchers' attention to SPPS in recent years. Most of the research on SPPS focusses on the output current's peak value and pulse width, the main switch's suppression of the open-circuit voltage, the multimodule SPPS's parallel discharge, and its use in different applications. The open-circuit voltage across the opening switch poses a significant threat to its capacity to turn off current. Because full-controlled current semiconductor switches function at a limited level, expanding a single-module IPPS to a higher-level current is difficult (Liebfried, 2017; Pokryvailo et al., 1999; Schoenbach et al., 1984; Yu and Liu, 2017). It is significant to remember that different approaches have been tried to remove the barrier (Ma et al., 2015; Yu and Chu, 2013). A high-temperature superconducting pulsed power transformer (HTSPPT) used in SPPS may produce an incredible pulse current that is several times larger than the energy storage current in addition to establishing superconducting magnetic energy storage (Li et al., 2012; Li, et al., 2016a, 2016b; Stoica et al., 2016).

Where Lu et al. (2020) proposed a three-winding pulse transformer (TWPT)-based IPPS to overcome the difficulty of reducing overvoltage across the opening switch and getting higher load currents. The residual energy is also rather significant, even though the solutions mentioned above are capable of producing high-amplitude current pulses. To capture and reuse the residual energy, (Liang et al., 2020) introduced a capacitor with a bridge-type switching circuit to improve the main switch-over voltage problem, as well as to capture the residual energy. The addition of a capacitor to the switching sequence improved the circuit's performance and captured leftover energy. However, a complex switching circuitry is proposed to solve the issue (Lu, 2020; Lu et al., 2020; Lu et al., 2021a) and design SPPS that can capture and reuse the residual energy, using an additional capacitor to faster the process of capturing residual energy. The circuit topologies mentioned above can capture and reuse the energy captured in the next cycle; however, they are limited to the peak value of the output current and repetitive operation, and there is also room for improvement in the energy recovery process. To address the high output peak current with residual energy recovery, in this work, a TWPT with two primary superconducting windings with a single copper-based winding is used instead of the double winding pulse transformer which is used in Li et al. (2016 a, b), an additional capacitor is used in the switching circuitry to capture the residual energy which was not addressed in the previous work and taking advantage of the features of HTS TWPT for getting high load current peaks by having two superconducting primary windings. This work provides a detailed theoretical analysis and introduction to enhance the operation and methodology of HTSPPS. Simulations are carried out to demonstrate the improved HTSPPS's practicality, and the effects of TWPT with two energy storage capacitances on the trigger delay time of the output current, and the repetitive rate of recovered energy are examined. The results of the simulation indicate that the inclusion of an additional capacitor in the proposed circuit topology enhances the current amplification factor, and it also recovers more residual energy than before.

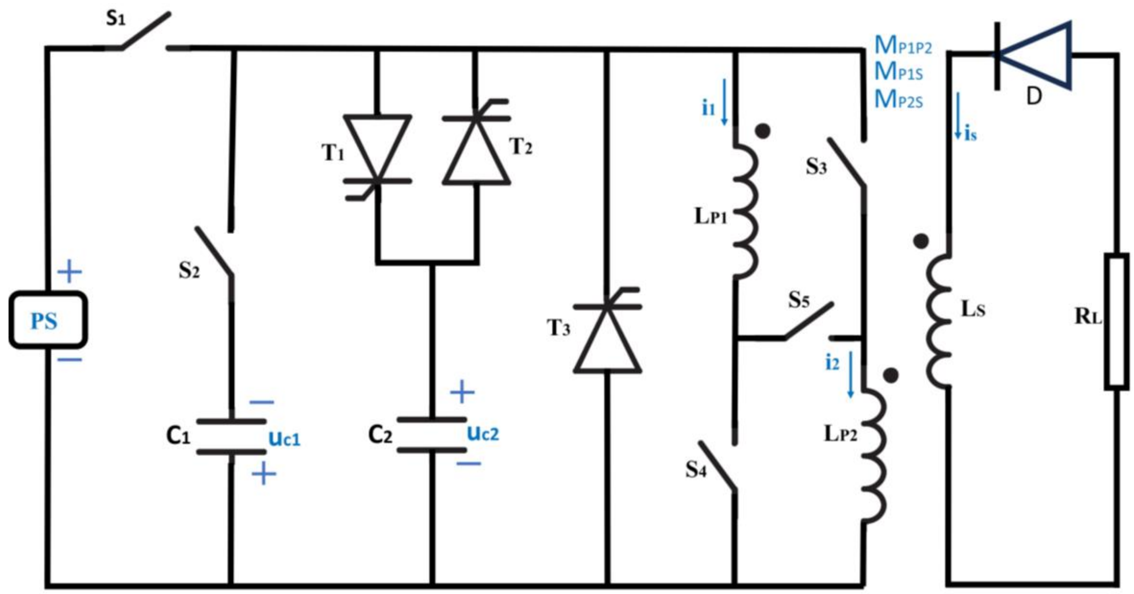

Figure 1. Modified circuit topology for SPPS using TWPT.

2. Model Description and Theoretical Analysis

The modified circuit topology of SPPS with TWPT is shown in **Figure 1**. TWPT is composed of one secondary winding made of copper and two primary superconducting windings. Parallel discharging and serial charging processes use Bi2223/Ag-based superconducting primary windings as energy storage devices. Two capacitors are utilized in an anti-parallel operation; one is switched by two thyristors using an anti-parallel switching technique, the other by a switch S_2, and a thyristor is also present in the freewheeling portion. This article assumes that all switches are perfect switches, that is, that all switches are turned on or off immediately and that their dynamic features such as voltage drop, maximum current, voltage, and other parameters of the switching component are not considered to make the analysis easier.

Air core TWPT has three windings L_1, L_2, and L_S with three mutual inductances between them M_{L1L2}, M_{L1Ls}, and M_{L2Ls}. Each superconducting winding L_1 consists of three superconducting coils $L_{1.1}$, $L_{1.2}$, and $L_{1.3}$, and L_2 consists of $L_{2.1}$, $L_{2.2}$, and $L_{2.3}$ and the secondary winding has two coils L_{S1} and L_{S2}, as shown in **Figure 2.** The superconducting coils are stacked in a sandwich-type configuration in which two superconducting coils are stacked, one from the L_1 winding and the other from the L_2 winding, where a copper-based coil is placed on the top, the sequence of stacked coils from bottom to top is $L_{1.1} \rightarrow L_{2.1.} \rightarrow L_{S.1.} \rightarrow L_{1.2.} \rightarrow L_{2.2.} \rightarrow L_{S.2.} \rightarrow L_{1.3.} \rightarrow L_{2.3}$. The winding pattern of three coils in the superconducting windings L_1 and L_2 with two copper-based coils in the copper winding L_S is shown in **Figure 2.**

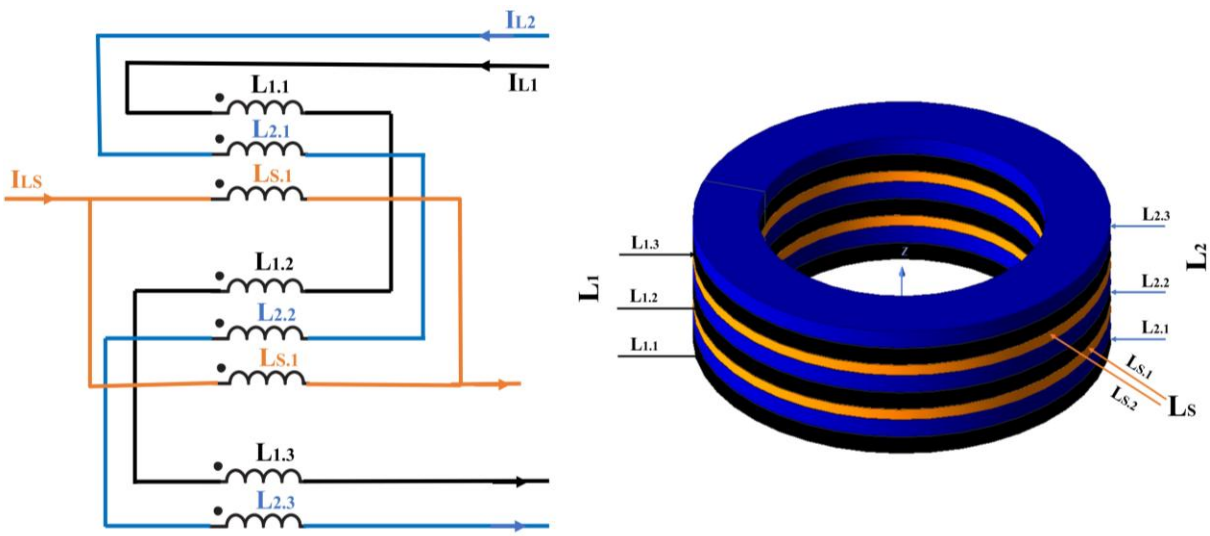

Figure 2. Connection pattern and structure of TWPT for HTSPPS.

The $L_{1.1}$, $L_{1.2}$, and $L_{1.3}$ are connected serially, the same for the L_2 windings and the secondary L_S windings connected parallelly. Each primary superconducting coil consists of 68 turns, creating a winding of 204 turns of primaries L_1 and L_2, while the secondary coils have 6, 6 turns connected in a parallel configuration to form the secondary winding 'L_S'. The dimensions and parameters of TWPT are given in **Table 1** and **Table 2** by finite element-based simulation.

Table 1. TWPT dimensions.

Material		Outer radius (mm)	Inner diameter (mm)	Height (mm)	Turns
Superconducting Bi2223/Ag	$L_{1.1}$ to $L_{1.3}$	100	70	10	68
Superconducting Bi2223/Ag	$L_{1.1}$ to $L_{1.3}$	100	70	10	68
Copper	$L_{S.1}$ and $L_{S.2}$	100	70	6	6

Table 2. Circuit parameters.

Parameters	Value
Primary power source P_S	120 V
Charging current Io	117A
Capacitor C_1	120uF
Capacitor C_2	30uF
Primary inductors L_1, L_2	5.31mH, 5.31mH
Secondary inductor Ls	12uH
Mutual inductances M_{L1L2}, M_{L1S}, M_{L2S}	3.1mH, 2.2mH, 2.2mH
Coupling coefficient	0.95
Load resistance	1.5mR
Operating frequency	25Hz

These five phases, which are represented in **Figure 3**, charging, discharging, energy recovery, freewheeling, and energy storage cover the working process. In the following study, the voltage drops and loss of thyristors and diodes are ignored to make the analysis easier.

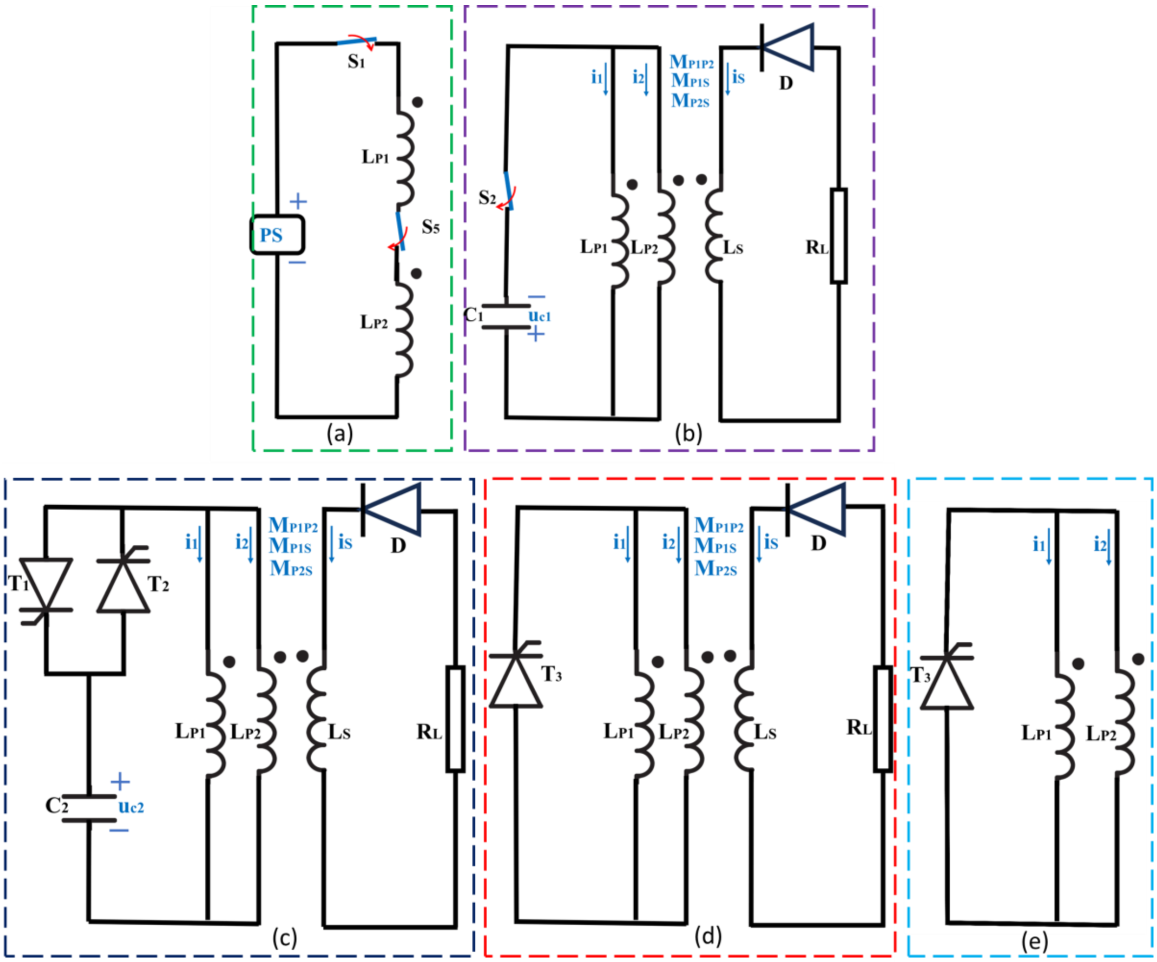

Figure 3. Working process of modified SPPS using TWPT (a) charging phase, (b) discharging phase, (c) energy recovery phase, (d) freewheeling phase, (e) energy storage.

2.1 Phase 1 (Charging)

The charging phase of the first cycle begins with the primary switches S_1 and S_3 turned on, and the secondary inducer L_2 does not receive any current at first. After S_1 is turned on and the current in L_2 decreases to zero, except for the first cycle, the charging phase begins. The serial excitation of the primary inductors L_1 and L_2 is then initiated by the P_S power supply. During this phase "$P_S \rightarrow T_1 \rightarrow L_1 \rightarrow S_3 \rightarrow L_2 \rightarrow P_S$" as shown in **Figure 3**, the diode D connected to the load blocks the current flowing through the secondary loop, and the thyristors in the switching circuit are in the OFF state with switches S_1 and S_2 open. The charging phase is finished when the switches S_1 and S_3 are turned off, indicating that the charging current has reached the necessary value, and the charging state is expressed in Equation (1). The symmetrical construction and connection arrangements of TWPT allow us to get Equations (2)-(5), which is supported by the simulation findings listed above in **Tables 2** and **3**. Thus, the original stored energy E_0 can be written as Equation (6).

$$L_1 \frac{di_1}{dt} + L_2 \frac{di_2}{dt} = v(t) \tag{1}$$

$$L_1 = L_2 \tag{2}$$

$$M_{L_1s} = M_{L_2s} \tag{3}$$

$$L_t = L_1 + L_2 + M_{L_1L_2} \tag{4}$$

$$M = M_{L_1s} + M_{L_2s} \tag{5}$$

$$E_0 = \frac{1}{2}L_tI_0 = \frac{1}{2}(L_1 + L_2 + M_{L_1L_2})\, I_0 \tag{6}$$

2.2 Phase 2 (Discharging)

The power ON S_2, S_3, and S_4 starts the charging phase after the power OFF T_1 and S_3. This causes both primary inductors to run in parallel, as shown in **Figure 3**. Using the leakage flux of both inductors L_1 and L_2, the capacitor C_1 charges. There is an LC oscillation circuit created by both inductors L_1 and L_2 with capacitor C_1. The primary current, i_1, and i_2, rapidly decays because of the coupling effect, creating a significant pulse current in the secondary circuit. The primary inductor through " $L_1||L_2 \rightarrow C_1 \rightarrow T_2 \rightarrow L_1||L_2$" is discharged by the capacitor when its voltage, u_{c_1}, reaches its maximum value. As the currents i_1 and i_2 are reversed, the induced current continues to increase rapidly. When the current in the secondary reaches the maximum value, the third phase activates. The discharging phase equation is described as follows.

$$L_1\frac{di_1}{dt} + M_{L_1L_2}\frac{di_2}{dt} + M_{L_1S}\frac{di_S}{dt} + u_{c_1}(t) = 0 \tag{7}$$

$$L_2\frac{di_2}{dt} + M_{L_1L_2}\frac{di_1}{dt} + M_{L_2S}\frac{di_S}{dt} + u_{c_1}(t) = 0 \tag{8}$$

$$L_S\frac{di_S}{dt} + M_{L_1S}\frac{di_1}{dt} + M_{L_2S}\frac{di_2}{dt} + R_Li_S = 0 \tag{9}$$

$$C_1\,\frac{du_{c_1}(t)}{dt} = i_1 + i_2 \tag{10}$$

From **Table 2**, it is defined that L_1 and L_2 are identical; therefore, their discharge time will be the same, and they will have the same amount of current flowing through C_1 described as:

$$i_1 = i_2 \tag{11}$$

$$\frac{di_1}{dt} = \frac{di_2}{dt} \tag{12}$$

Adding Equations (7) and Equation (8) and simplifying the result can be expressed in Equation (13),

$$(L_1 + L_2 + 2M_{L_1L_2})\,\frac{di_1}{dt} + \left(M_{L_1S} + M_{L_2S}\right)\frac{di_S}{dt} + 2u_{c_1}(t) = 0 \tag{13}$$

where, Equations (9) and (10) an be described as:

$$L_S\,\frac{di_S}{dt} + \left(M_{L_1S} + M_{L_2S}\right)\frac{di_1}{dt} + R_Li_S = 0 \tag{14}$$

$$C_1\frac{du_{c_1}(t)}{dt} = 2i_1 \tag{15}$$

2.3 Phase 3 (Energy Recovery)

Thyristor S_2 is turned off and Thyristors T_1 and T_2 are turned on to begin the energy recovery phase. The reverse currents of the primary inductors, i_1, and i_2, discharge the additional capacitor C_2 via path "$L_{P1}||L_{P2} \rightarrow C_2 \rightarrow T_3 \rightarrow L_{P1}||L_{P2}$" The secondary current rapidly decays, while currents i_1 and i_2 quickly switch from reverse to forward flow, with path "$L_{P1}||L_{P2} \rightarrow C_2 \rightarrow T_4 \rightarrow L_{P1}||L_{P2}$" for current flow as shown in **Figure 3**. As a result, capacitor C_2 receives and stores the remaining energy. Following a half-LC oscillation period, the next stage begins when the capacitor voltage, u_{c_2}, reaches zero. Taking into account Equations (2), (3) and (11). The energy recovery phase equation is described as:

$$(L_1 + L_2 + 2M_{L_1L_2})\frac{di_1}{dt} + (M_{L_1S} + M_{L_2S})\frac{di_S}{dt} + 2u_{c_2}(t) = 0 \quad (16)$$

$$L_S\frac{di_S}{dt} + (M_{L_1S} + M_{L_2S})\frac{di_1}{dt} + R_L i_S = 0 \quad (17)$$

$$C_2\frac{du_{c_2}(t)}{dt} = 2i_1 \quad (18)$$

2.4 Phase 4 (Freewheeling)

Positive currents, i_1, and i_2, flow freely through the T_3 thyristor when turned on, which is achieved by turning off T_1 and T_2 and turning on T_3. While the secondary current decays, both primary currents i_1, and i_2 continue to rise through a path "$L_1||L_2 \rightarrow T_3 \rightarrow L_1||L_2$". When the secondary current reaches zero, the first phase begins. The freewheeling phase equation is described as

$$(L_1 + L_2 + 2M_{L_1L_2})\frac{di_1}{dt} + (M_{L_1S} + M_{L_2S})\frac{di_S}{dt} = 0 \quad (19)$$

$$L_S\frac{di_S}{dt} + (M_{L_1S} + M_{L_2S})\frac{di_1}{dt} + R_L i_S = 0 \quad (20)$$

2.5 Phase 5 (Energy Storage)

After the secondary current eventually decays to zero, the conversion capacitor C_1 and the primary superconducting inductors L_{P1} and L_{P2} recover and store the remaining energy. The equation is described as:

$$(L_1 + L_2 + 2M_{L_1L_2})\frac{di_1}{dt} = 0 \quad (21)$$

As described in Equation (21), some of the energy recovered in the primary inductors and in capacitor C_1, can be used for the next cycle. The energy recovered in all phases can be determined by the following equation.

$$E_r = \frac{1}{2}L_t i_r^2 + \frac{1}{2}C_1 u_{c_{1r}}^2 \quad (22)$$

where, the recovered valves for the primary current are denoted by i_r and the capacitor voltage by u_{C1r}.

Using the recovered energy, the HTSPPS energy efficiency can be increased for the subsequent cycle. The next cycle's charging procedure can use the energy that has been recovered in the primary inductor. The primary inductor will charge faster thanks to the current i_r. The energy of capacitor C_1 might be utilised during the subsequent cycle's discharging procedure. For the output current to reach its peak value and the primary current to decrease more quickly, the voltage u_{C1r} will speed up the discharging process.

Based on the analysis above, it is evident that the closing switches S_2, S_3, and S_4 require bidirectional half-controlled devices, similar to the antiparallel pairing of a diode and a thyristor, as illustrated in **Figure 3**. The opening switches S_1 and S_5 require fully controlled devices, such as IGBT. In addition, to prevent open circuits and short circuits, the opening and closing switches must be turned on or off simultaneously.

3. Simulation and Parametric Analysis

To demonstrate and prove the performance of the modified TWPT-based HTSPPS, simulations with parametric analysis are carried out. The circuit parameters are set according to **Table 1** and **Table 2**. The values of primary inductors L_1, L_2, and secondary inductor Ls are 5.3mH, 5.3mH, and 12uH, respectively, with a coupling coefficient of 0.95. The initial values of current, voltage and stored energy are set to 100A, 120V, and 68.8J, correspondingly the load resistance is set to be 1.5mΩ. The simulations are carried out by varying both capacitors C_1 and C_2 to get the optimum values for higher load currents and energy recovery; finally, the simulation is done to achieve a 25Hz repetitive rate. Trigger timing of all switches and thyristors is shown in **Figure 4**. By switching S_1 and S_5 in conduction, the primary current charges the superconducting primary side inductors in a series configuration. Switch off both switches after completion of the charging switch, first S_2, S_3, and S_4 are on to make the oscillation between the primary inductor and capacitor C_1, the detailed working process is detailed in the previous section.

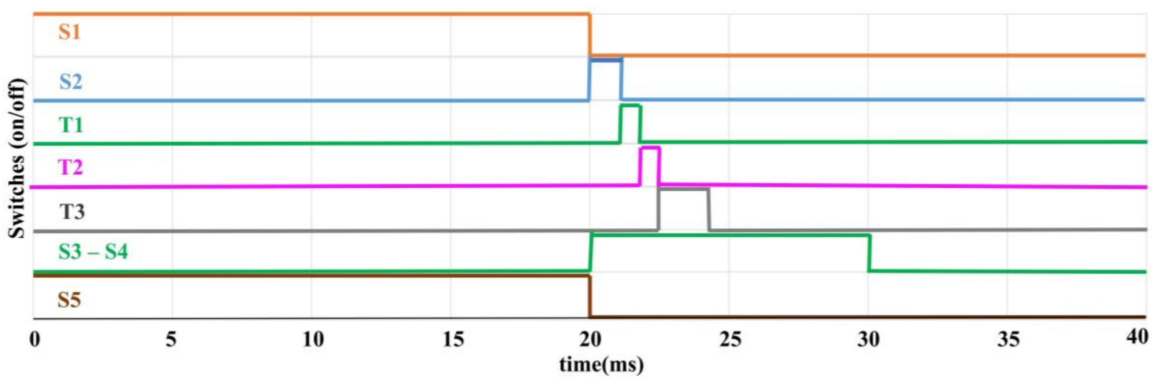

Figure 4. Trigger timing sequence of switches and thyristors.

The initial values of the C_1 and C_2 capacitors are 20 to 200uF, respectively. This process of selecting initial values ensures that the simulation initially mimics the actual operating environment of the circuit, even under complex conditions. The energy transfer method is simplified by selecting a charging and discharge time of 20ms and 10ms, respectively. The 25Hz frequency is used to complete the continuous operation compared to the smooth charging and discharging process because the inductive pulsed power supply faces continuous operation due to better charging and discharging. The literature that suggests repeated operation of a 20Hz power supply states that applications such as EML or firearms require continuous operation.

Since the circuit does not require any pre-charge, the initial voltage of the capacitor is set to zero. The trigger time for each switch and thrust is shown in **Figure 4**. By replacing S_1, S_5, and S_5 in the current, the main current imposes a superconductor's main side pointer in the series sequence. Turn off both switches after the charging process is completed. Turn on the S_2, S_3, and S_4 switches to create an oscillation between the main indicator and the C_1 capacitor. The specific operation of this switch is described in the previous section.

3.1 Parametric Analysis by Fixing C_1

In this section, we examine the impact of varying the capacitance of capacitor C_1 on the performance of a modified high-temperature superconducting pulsed power supply (HTSPPS), while keeping the capacitor C_1 fixed at 100μF. The C_2 values were adjusted to 20, 50, 80, 120, 150, 180, and 200μF. The results demonstrated that the primary current curves (i_1 and i_2) maintained complete consistency due to synchronized discharge and stable circuit parameters.

Figure 5 illustrates the modeling behaviour of the modified HTSPPS with different C_2 values. It was observed that the change in capacitance of C_2 had a minimal effect on the voltage of capacitor C_1 and the load current. This stability suggests that the primary influence of C_2 variation lies in other aspects of the system rather than in altering the voltage of C_1 or the overall load current. At a low capacitance of 20μF for C_2, a very high pulse was generated, potentially affecting the connected thyristors. However, at capacitance values of 50, 80, and 100μF, the voltage across C_2 (u_{C2}) represented half the original voltage and the recovered current was significant. As the capacitance of C_2 increased, the voltage U_{C2} decreased. This indicates an optimal performance range for C_2, where the system operates efficiently without risking component damage. The discharge process of the modified HTSPPS was notably rapid, taking only 1 millisecond, while the charging current decays to -91A as C_2 increases with the decay pulse reaching -70A. This rapid discharge and subsequent reduction in charging current highlight the system's capability to quickly stabilize, which is crucial for applications requiring fast energy pulses.

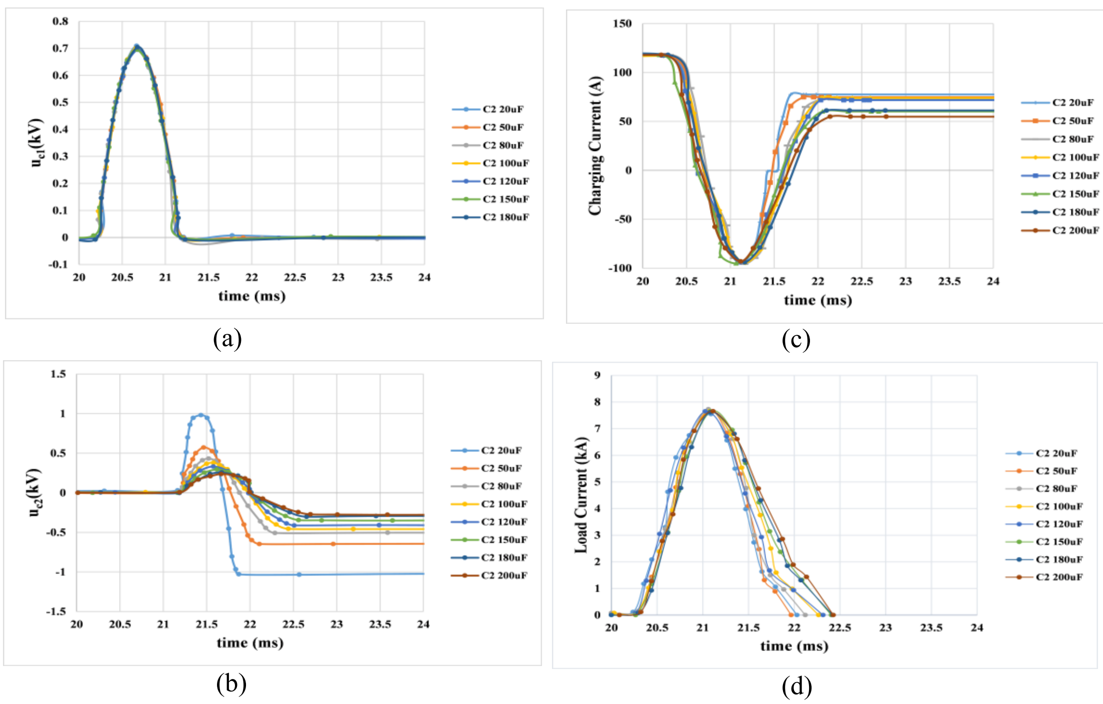

Figure 5. Simulation results with fixed C_1 (a) Capacitor C_1 voltage (b) Capacitor C_2 voltage (c) Charging current (d) load current.

The comprehensive results of the simulation are displayed in **Table 3**, with C_1 fixed at 100uF, the load current, recovery current, and voltage across the capacitors by varying C_2 from 20uF to 200uF are given. Data shows that the load current remains stable at a value of 7.5kA with the variation, which indicates the circuit's robust ability to handle the current. The recovered current in the primary inductor is observed to decrease by increasing C_2 from 79A to 56A. The trend of recovered current in primary inductors shows that a small value of C_1, such as 20 to 30uF, is more beneficial in the improvement of the overall efficiency of the system.

The circuit characteristics mentioned above show that the load current of the circuit behaves consistently and is sensitive to changes in the recovered current on C_2 and its voltage dynamics. For applications like high-current pulse generators, the system's dependability is shown by the output current's stability across a range of capacitances. Furthermore, the trend in systems that consider capacitor voltages and recovered current in primary inductors provides information on energy efficiency and charging-discharge processes in circuits and directs optimisation efforts to enhance the performance of high-current applications.

Table 3. Results by varying C_2 with C_1 =100uF.

C_2	1st	2nd	3rd	4th	5th	6th	7th	8th
	20uF	50uF	80uF	100uF	120uF	150uF	180uF	200uF
i_L (kA)	7.5	7.5	7.5	7.5	7.5	7.5	7.5	7.5
i_r (A)	79	75	74	74	72	59	58	56
u_{c2} (V)	-100	-650	-510	-460	-410	-350	-300	-280
u_{c1r} (V)	0	0	0	0	0	0	0	0

3.2 Parametric Analysis to Fix C_2

In this analysis, capacitor C_2 was kept constant at 50µF while capacitor C_1 was varied from 20µF to 200µF to investigate its impact on the system performance. As illustrated in **Figure 6**, increasing the capacitance of C_1 resulted in a noticeable reduction in the peak voltages between the two capacitors (u_{C1} and u_{C2}) and the load current (i_L). This observation is crucial as it indicates that higher values of C_1 lead to lower peak voltages and currents, potentially reducing the stress on circuit components and improving the overall system reliability. Here, the values of capacitor C_1 are adjusted to 20, 50, 80, 120, 150, 180, and 200uF, respectively, and the value of capacitor C_2 is set to 50uF. As capacitor C_1 increases, **Figure 6** shows the peak values of capacitor voltages u_{C1}, u_{C2}, and load current i_L drop.

Figure 6 illustrates how the discharge time increases from 0.5ms to 1.2ms, and the lowest value of the discharge current decreases from -91 A to -70 A. As capacitor C_1 increases, the discharge current decreases from -91 A to -70 A.

However, as **Figure 6** illustrates, the recovered voltage u_{C1r} has higher values when the capacitor C_1 is 20uF, then drops to a low level when the capacitor is 40uF, then u_{C1r} increases with an increase in the energy recovered in the primary inductors. There is a higher capacitor voltage peak at 20uF, which can damage the main switch due to higher stress. However, considering a C_1 value greater than 40uF, the simulation trend shows the stability of the recovered voltage when C_1 has higher values. Detailed parametric values obtained from the simulation results are illustrated in **Table 4**.

The inductor current i_L steadily decreases from 8.1 kA to 6.5 kA, indicating that higher capacitance values result in lower current through the inductor. The recovered current i_r exhibits a more complex pattern: it is exceptionally high at 91 A when C_1 is 20µF, then fluctuates, and gradually decreases as C_1 increases. The voltage across C_1 during recovery u_{c1r} shows dramatic variations, starting very high at 1180 V, dropping to negative values, and eventually increasing back to positive values as C_1 increases. This suggests that smaller C_1 values cause greater voltage swings, which may hinder the stability of the system, while larger values stabilize the voltage.

Table 4. Results by varying C_1 and C_2 = 50uF.

C_1	1st	2nd	3rd	4th	5th	6th	7th	8th
	20uF	50uF	80uF	100uF	120uF	150uF	180uF	200uF
i_L(kA)	8.1	8	7.7	7.6	7.4	7.35	6.9	6.5
i_r(A)	91	54	69	76	78	72	64	56
u_{c1r} (V)	1180	-370	-162	0	150	300	360	390
u_{c2} (V)	-118	-480	-590	-640	-650	-620	-560	-300
Total Energy Recovery	70	23.4	31.663	39.565	43.025	42.26	39.73	36.69

The voltage across C_2 (u_{c2}) is consistently negative throughout. Usually, its magnitude increases, peaks as C_1 rises, and then progressively decreases once again. This implies that C_2 is in a continuous discharge phase or is being charged with opposite polarity. The overall energy recovery is substantial at 70 J when C_1 is 20uF. C_1 drops to 23.4 J, its lowest value at 50uF. C_1 rises to a maximum of 43.025 J at 120uF. However, because of the instability at 20uF, the system seems to recover more energy at 120uF as shown in **Table 4**. This nonlinear connection shows that the system performs best at 120uF, showing that there may be a perfect C_1 value for maximizing energy recovery. These insights are crucial for optimizing circuit performance in applications that require efficient energy recovery.

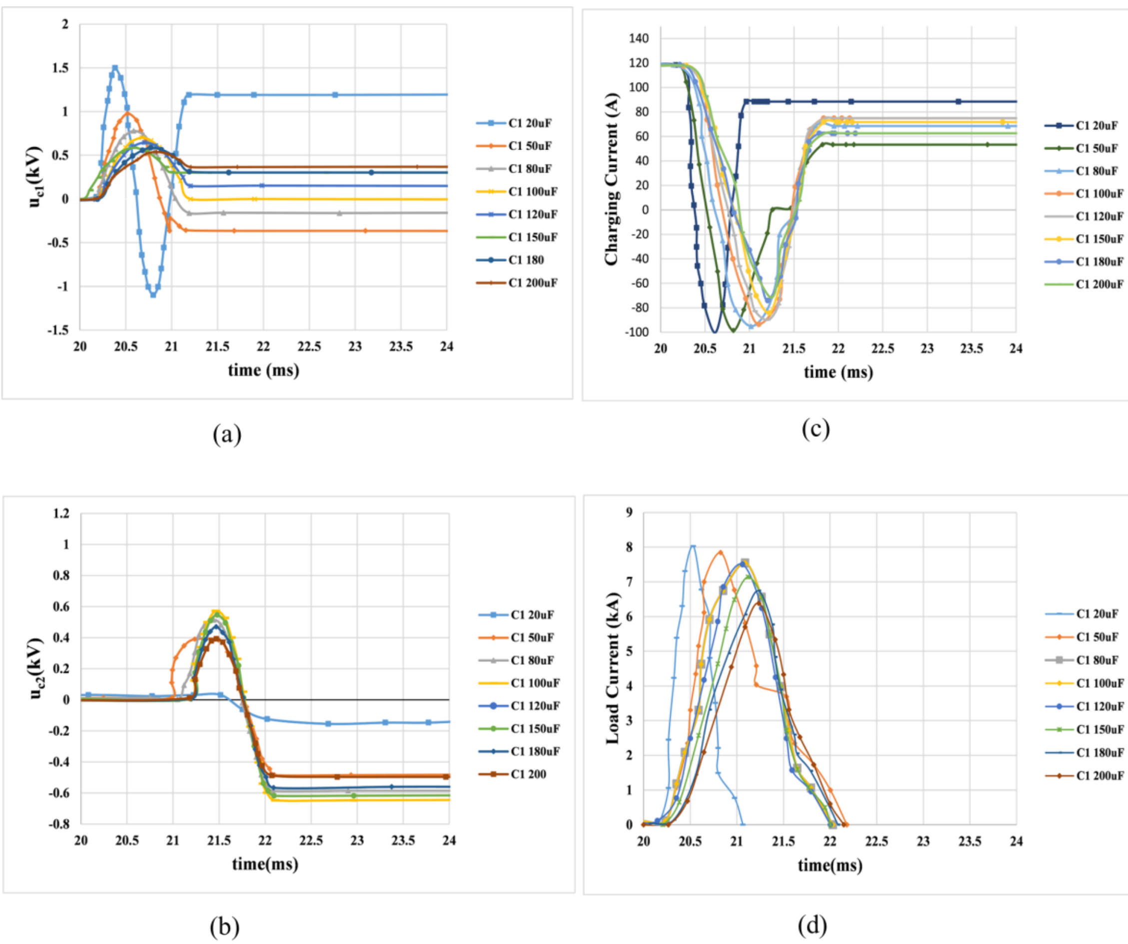

Figure 6. Simulation results with C_2 fixed (a) capacitor C_1 voltage, (b) capacitor C_2 voltage (c) charging current, (d) load current.

3.3 Parametric Analysis of both C_1 and C_2

The recovered voltage in C_1 across different capacitance values of C_1 and C_2 reveals a detailed pattern of behaviour, as shown in **Figure 7**. The recovery current (i_r) of the primary inductor was measured over a range of C_1 and C_2 values. Current i_r was detected around 92A for all C_2 values for C_1 = 20uF, indicating steady recovery at lower capacitance levels. A range of 71A to 75A was obtained for different C_2 values when C_1 increased to 30μF, suggesting a possible relationship between increased recovery efficiency and C_2, i_r ranged from 33A to 59A for C_2 values of 10 to 100uF as C_2 was 50uF, demonstrating a positive connection with the increase in C_1, i_r stayed between 72.4A and 78.4A in C_1 (100μF), indicating a steady recovery dynamic.

The recovery current decreases with an increase in the value of C_1, as evidenced by the stabilisation of the recovery current at 54-56.8 A with C_1 (200uF). These results highlight the importance of increasing C_1 and C_2 values to manage current and overall circuit maintenance performance. The high capacitance value can improve the voltage stability and control load current while generally reducing the maintenance current. According to a detailed examination of the data at hand, C_1 (120uF) and C_2 (30uF) are the best values to increase the load current of the circuit and present a useful recovery current. In this setup, the recovery voltage of 147V C_1 is higher than most C_1 values, except 20uF. This voltage level reduces sudden changes and improves the stability of the circuit by ensuring a balanced energy recovery process. In addition, the design load current exceeds 7501 A, which is one of the most well-known stable values. This highlights the ability of high-load current circuits to maintain high current loads without suffering performance losses, which is essential for high-demand applications.

When C_1 is at 20 µF, the recovered voltage remains stable at approximately 1159-1160 V, irrespective of the value of C_2. However, a high voltage spike occurs at this value. As C_1 increases to 30 µF, there is a noticeable shift, with the recovered voltage starting at 214 V when C_2 is 10µF and gradually rising to 300 V as C_2 reaches 100µF. This positive correlation suggests enhanced energy storage and recovery as both capacitances increase. When C_1 is 40µF, the voltage recovery turns negative, starting at -419 V and gradually decreasing, indicating a change in the discharge dynamics of C_1. This negative trend continues until C_1 reaches 100µF, where the voltage stabilises around -5 V. Beyond this point, at C_1 values of 120µF and higher, the recovered voltage becomes positive again, increasing up to 390 V for C_1 at 200uF. This suggests that higher C_1 values enable more efficient voltage recovery, likely due to improved charge-discharge cycles.

Regardless of C_2 levels, the load current is constant at approximately 8134 A when C_1 is 20uF, showing that lower C_1 values may effectively support large current loads. Lower C_1 values, on the other hand, would cause a strong voltage pulse that, under extreme stress, might harm the switch S_2. Load current remains constant at 8111A when C_1 is increased to 30µF but decreases to 7483A when C_2 is increased to 80µF. The load current for C_1 at 50uF remains at 7956A, indicating that changing C_2 has little effect. The load current steadily drops as C_1 increases and stabilises between 6527 and 6544A at 200uF, showing that higher C_1 values often result in lower load current due to higher capacitive reactance and energy storage requirements.

The recovery current (i_r) of the primary inductor was measured over a range of C_1 and C_2 values. Current i_r was detected around 92A for all C_2 values for C_1 = 20uF, indicating steady recovery at lower capacitance levels. A range of 71A to 75A was obtained for different C_2 values when C_1 increased to 30µF, suggesting a possible relationship between increased recovery efficiency and $C_{2,}$ i_r ranged from 33A to 59A for C_2 values of 10 to 100uF as C_2 was 50uF, demonstrating a positive connection with the increase in $C_{1,}$ i_r stayed between 72.4A and 78.4A in C_1 (100µF), indicating a steady recovery dynamic.

The current i_r decreases with an increase in the value of C_1, as evidenced by the stabilisation of the recovery current at 54-56.8 A with C_1 (200uF). These results highlight the importance of increasing C_1 and C_2 values to manage current and overall circuit maintenance performance. The high capacitance value can improve the voltage stability and control load current while generally reducing the maintenance current. According to a detailed examination of the data at hand, C_1 (120uF) and C_2 (30uF) are the best values to increase the load current of the circuit and present a useful recovery current. In this setup, the recovery voltage of 147V C_1 is higher than most C_1 values, except 20uF. This voltage level reduces sudden changes and improves the stability of the circuit by ensuring a balanced energy recovery process. In addition, the design load current exceeds 7501 A, which is one of the most well-known stable values. This highlights the ability of high-load current circuits to maintain high current loads without suffering performance losses, which is essential for high-demand applications.

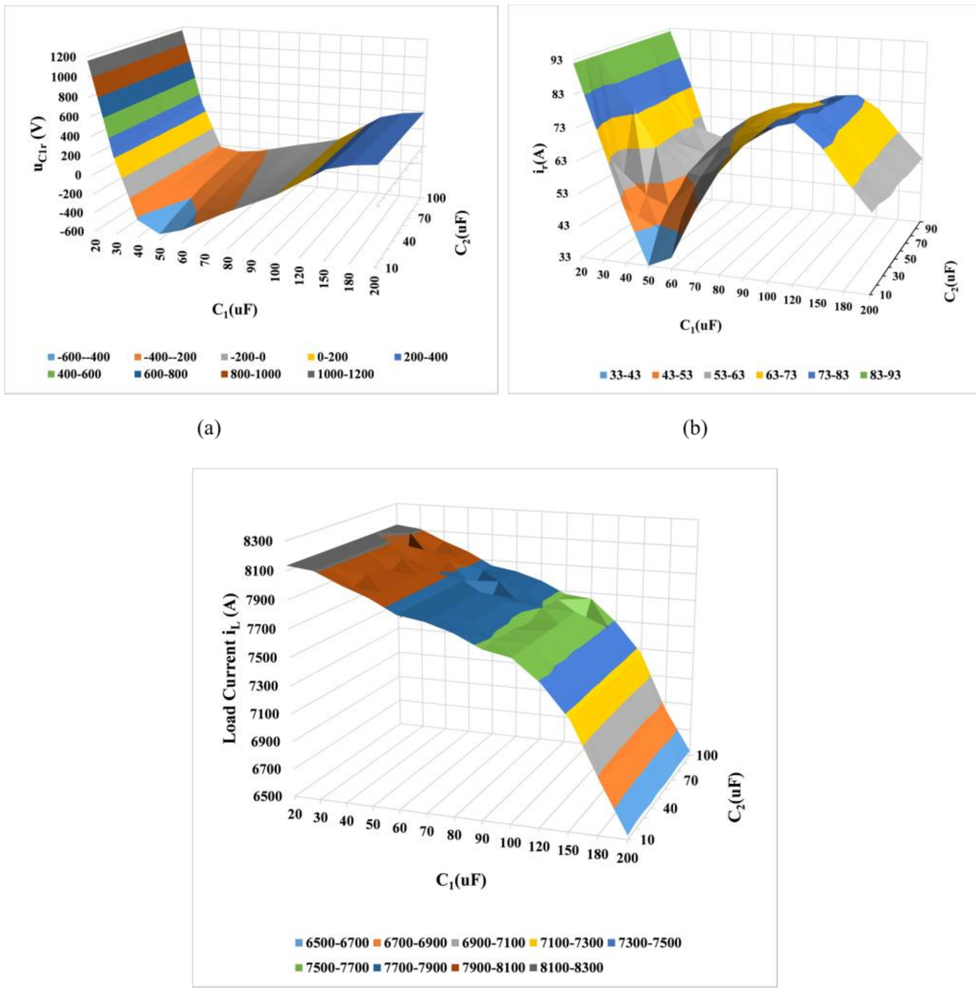

(a) (b)

(c)

Figure 7. Effect of C_1 and C_2 on (a) recovered primary current, (b) recovered voltage in C_1, and (c) load current.

The recovery current in the lead indicator and the energy recovered in capacitor C_1 is greater when comparing the capacity of 20uF to 120uF. On the other hand, because the S_2 switch is under increasing pressure, an unstable switch circuit is produced near the 20uF limit. At 120uF, a second higher peak is observed, indicating the maximum recovery current and energy reuse. It can improve efficiency and reduce energy loss. Due to the high, stable, and large load current, recovery voltage, and effective recovery current, C_1 (120uF) and C_2 (30uF) show an excellent balance between performance and efficiency. When conditions call for high circuit performance, this value of capacitance provides reliable and effective results. Applications that require strong current management and energy efficiency benefit greatly from their use. To maintain the capacitive-to-inductive energy storage ratio and facilitate the fast charging and discharging process required for continuous operation, it is recommended to choose the lower capacitance of C_2 (30uF).

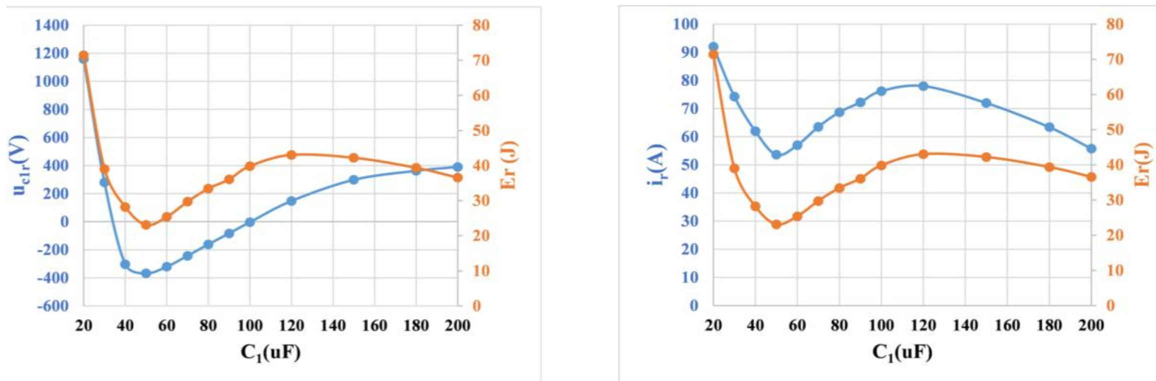

(a) (b)

Figure 8. Optimal value of C_1 (a) recovered voltage in C_1 and recovered energy (b) recovered primary current and recovered energy.

3.4 Modelling of 25Hz Repetitive HTSPPS

A study of the properties of the HTSPPS was conducted by modelling the charging and discharging processes of the 25 Hz repeated HTSPPS as shown in **Figure 9**. As shown in **Figure 8** the high recovery current and capacitor voltage is at a capacitance of 120uF of C_1. Therefore, the values of the capacitors that are being used in the simulation are 120uF and 30uF for capacitors C_1 and C_2, respectively. These values are the optimum values observed from the simulation results. At first, there is no capacitor voltage and there is no primary current. Due to the consistent circuit characteristics and synchronised discharge, the improved HTSPPS displays total consistency in its two primary current curves (i_1 and i_2). Every charge-discharge cycle comprises two phases: a 20-ms charging phase and a 10-ms discharging phase.

The reason for this is that in the first cycle, the primary inductor's charging period (t_1) was 20 milliseconds. 400 milliseconds, or ten charge-discharge (t_{c1} to t_{c10}) time cycles are denoted, where is the chosen simulation length. The simulation trigger sequence of the switches and thyristors is shown in **Figure 4**. During the charging phase, the waveform of primary currents i_1 and i_2 changes; the other waveforms, the voltage and current, remain constant. The current waveforms i_1 and i_2 of the tenth cycle t_{c10} are shown in **Figure 9**. Since every waveform associated with current and voltage changes during the discharging cycle, they are all involved. The voltage and current waveforms for the first three milliseconds are the only ones provided by all discharge cycles. The previous simulation results show that when the capacitor voltage u_{C1} is initially zero, the load current i_L reaches its maximum value in 1.0ms. This indicates that switch S_2's ideal on time is 1.0ms. For each of these ten cycles, Switch S_2's set on time is 1.0ms. Because the initial voltage u_{C1} is zero, which prevents the load current from reaching its peak value when switch S_2 is opened, there will be a lower value of the peak load current. Following a few cycles, the peak value of the output current steadily reaches a stable value of 7.82kA, while the final value of the capacitor voltage u_{C1} eventually reaches a stable value of 245V, as shown in **Table 5.**

Table 5. Parametric response at 25Hz repetitive rate.

	t_{cycle1}	t_{cycle2}	t_{cycle3}	t_{cycle4}	t_{cycle5}	t_{cycle6}	t_{cycle7}	t_{cycle8}	t_{cycle9}	$t_{cycle10}$
i_{Lpeak}(ms)	21.21	61.22	101.22	141.21	181.20	221.12	261.21	301.2	341.2	381.2
i_L (kA)	7376.9	7800.5	7822	7814	7800	7825	7820	7800	7810	7820
i_1 and i_2 (A)	116.9	116.9	116.9	116.9	116.9	116.9	116.9	116.9	116.9	116.9
u_{C1} (V)	237.2	244.3	250	260	244	251	259	245	246	244.1

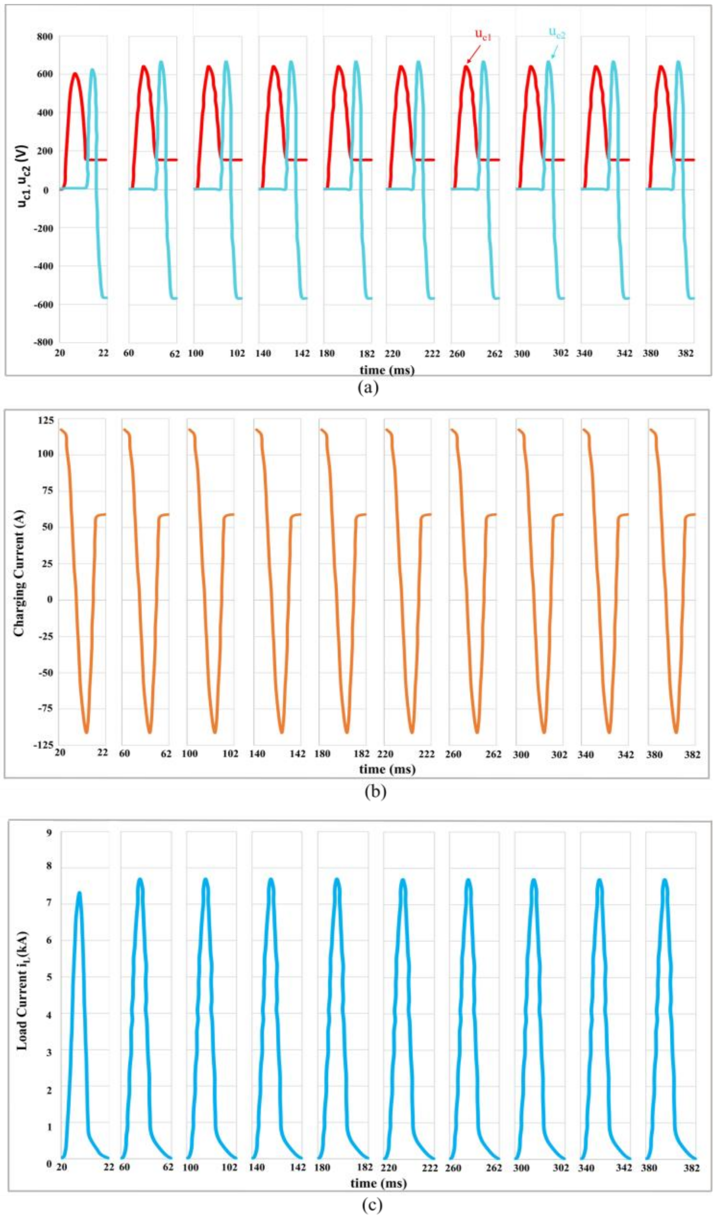

Figure 9. Simulation result 25Hz of HTSPPS (a) capacitor voltage u_{c1} and u_{c2} (b) charging current (c) load current.

Initially, there is no precharged energy in the primary inductors, and, as well as in the capacitors during the first cycle, the output current peaks lower, and the capacitor voltage u_{C1} eventually drops. After the first-time cycle t_{c1} has its highest and lowest values, the maximum value of the capacitor u_{C1} barely fluctuates by 8.8%. There is only a 5.7% difference between the maximum load current value at its highest and lowest values. The first capacitor voltage, u_{C1}, and the lowest initial stored energy of the first cycle are the main causes of these discrepancies. After a few cycles, the capacitor voltage, u_{C1}, ultimately reaches a stable value of 245.0 V. The load current peak value quickly leans to a stable value of 7.82kA. According to the simulation's findings, a modified HTSPPS with a selected trigger period can reliably provide output features like multiple currents.

4. Results and Comparative Analysis

Detailed parametric analysis of the superconducting pulsed power supply based on three windings is presented. The analysis starts with varying capacitor C_2 while fixing capacitor C_1 to 100uF, it was observed that there is no recovered energy present in capacitor C_1, only some recovered energy is present in the primary inductors and capacitor C_2. However, while fixing C_2 to 50uF and varying C_1, it is observed that energy is being recovered in the primary inductors, C_2 and C_1. A higher value of energy recovery was observed where there is less voltage stress on the main switch when C_1 is 120uF. Simulation by changing both C_1 and C_2 shows that there is very little effect on the load current and energy recovery by varying C_2, however, starting C_1 from 40 to 200uF, the results show that the maximum energy recovery and load current were obtained when C_1 is 120uF.

With the capacitor values of 120uF and 30uF of C_1 and C_2, respectively, the circuit was simulated with the same charging current and compared with the previous work. The results show that the proposed TWPT-based HTSPPS based on simulation results and the data available in the literature (Lu et al., 2020; Lu et al., 2021a; Lu et al., 2021b)_show a degree of agreement that is listed in **Table 6**. The maximum load current value of the TWPT-based topology (Lu et al., 2020) is 7.62kA with a current multiplication of 76, which is the maximum of all other topologies because the two primary inductors are discharged in a parallel configuration, making the load current higher. The proposed circuit's peak value is like (Lu et al., 2020) and attains a higher value of 6.67kA with a coefficient of current multiplication of 66.75. Both topologies in Lu et al. (2021a) and Lu et al. (2021b) have lower load current peaks of 4.86, and 4.95kA with coefficients of current multiplication are 48.6 and 49.5 respectively. The recovered energies in Lu et al. (2021a) and Lu et al. (2021b) are 35.6J, and 33.85J which are lower than the proposed circuit, which has a recovered energy of 36.652J.

Table 6. Comparison of parameters.

Parameters	Lu et al. (2020)	Lu et al. (2021a)	Lu et al. (2021b)	Proposed circuit
Primary inductors, i_{p1}, i_{p2}	4.575mH, 4.575mH	12.7mH	12.7mH	5.31mH, 5.31mH
The secondary inductor i_s	8.29uH	8.64uH	8.64uH	12uH
Coupling coefficient k	96%	92%	92%	90%
Primary charging current I_0 (A)	100	100	100	100
Load current i_L(kA)	7.62	4.86	4.95	6.67
Recovered current in the primary inductor i_r (A)	---	68.5	67.9	70
Recovered voltage in capacitor C_1 u_{C1r} (V)	----	400	420	225
Initial energy E_0 (J)	89.685	63.85	63.85	68.8
Total recovered energy E_r (J)	-----	35.6	33.85	36.652
Repetitive rate	-----	------	20Hz	25Hz

The total energy efficiency of the circuit is based on the energy transferred to the load, which can be observed in the load current peak, second, how much energy is being captured and reused again is shown as the recovered energy in the capacitor, and thirdly how much energy is lost. The results obtained from the proposed circuit topology show a better load current peak of 6.67kA, higher recovered energy of 36.652J, and a better performance in attaining a higher current peak of 29.6% and recovering higher energy of 2.9% than (Lu et al., 2021a; Lu et al., 2021b), and having lower current peaks of 13.3% than (Lu et al., 2020) but better in recapturing the leftover energies as there is no energy recovery noticed in Lu et al. (2020). The proposed TWPT-based HTSPPS also has a higher repetitive rate of 25Hz, whereas previous topologies attain 20Hz repetitive rates (Lu et al., 2021b). **Figure 10** shows a bar chart containing a detailed parametric comparison of all four topological circuits.

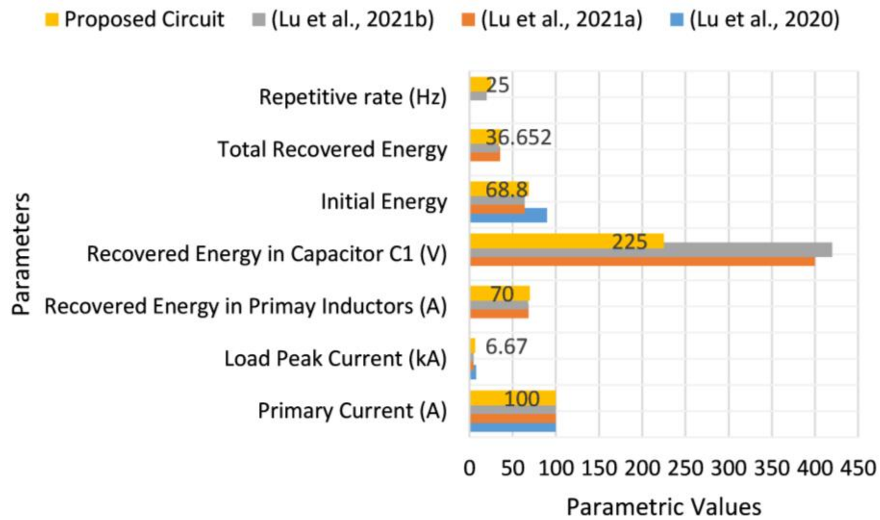

Figure 10. Parametric comparison chart of different topologies.

5. Conclusion

This work proposes and investigates a TWPT-based HTSPPT that operates continuously at 25 Hz and recovers residual energy. The impacts of capacitors on the output characteristics of HTSPPS with TWPT, which operates on the principle of parallel discharging and serial charging and features superconducting primary windings, have been thoroughly studied. The results of modelling and theoretical research show that the proposed circuit delivers a higher peak current of 6.67kA and recovers more leftover energy than traditional circuits. The recovered energy can shorten the charging period, increase the working frequency, give the improved HTSPPS one more cycle, and contribute to a higher load current peak. Due to the increase in recovered residual energy and the higher energy transferred to the load, the overall efficiency of the system is increased from the previous work. Reducing the rising time and raising the output current peak value is possible by accelerating the primary current attenuation through the first capacitor voltage. The proposed circuit topology with better energy efficiency and higher repetition rate can be a step forward in the development of repetitive use of EML and railguns. The modified HTSPPS makes the switching mechanism more complicated and places tight limitations on the switches' on and off times. With a superconducting TWPT installed in a foam cryo dewar, it has six connection links to external devices, adding more complexity, which may pose difficulties in practical implementation. Superconducting Materials require complex, sophisticated cooling systems and frequent maintenance to avoid material losses and damage, which may increase costs and challenges for larger applications. Future work will focus on improving the modified HTSPPS and conducting experiments for verification.

Conflict of Interest

There is no conflict of interest.

Acknowledgments

The authors would like to thank the Malaysian Ministry of Higher Education for research funding with grant number FRGS/1/2023/TK07/UTM/01/4.

For the correspondence, please contact the **corresponding author(s)** at ayaz@graduate.utm.my (Ayaz Ahmed), and hasmat.malik@gmail.com (Hasmat Malik).

References

Bae, S., Kwasinski, A., Flynn, M.M., & Hebner, R.E. (2010). High-power pulse generator with flexible output pattern. *IEEE Transactions on Power Electronics*, *25*(7), 1675-1684. https://doi.org/10.1109/tpel.2010.2041012.

Bluhm, H. (2006). *Pulsed power systems : principles and applications*. Springer: Berlin/Heidelberg, Germany. ISBN: 978-3-540-26137-7(p), 978-3-540-34662-3(e). https://doi.org/10.1007/3-540-34662-7.

Dedié, P., Brommer, V., & Scharnholz, S. (2011b). Twenty-stage toroidal XRAM generator switched by counter current thyristors. *IEEE Transactions on Plasma Science*, *39*(1), 263-267.

Dedié, P., Brommer, V., Badel, A., & Tixador, P. (2011a). Three-stage superconducting XRAM generator. *IEEE Transactions on Dielectrics and Electrical Insulation*, *18*(4), 1189-1193.

Kanter, M., Cerny, R., Shaked, N., & Kaplan, Z. (1993). Repetitive operation of an XRAM circuit. In *Ninth IEEE International Pulsed Power Conference* (pp. 92). IEEE. Albuquerque, NM, USA. https://doi.org/10.1109/ppc.1993.512884.

Li, H., Li, Z., Zhang, C., Hu, Y., Gao, M., & Chen, Y. (2018a). Experimental research on single module repetitive inductive pulsed power supply with fixed-frequency operation. *IEEE Transactions on Applied Superconductivity*, *28*(8), 1-6. https://doi.org/10.1109/tasc.2018.2874422.

Li, H., Wang, Y., Zhu, Y., Wu, R., Dong, L., & Dou, K. (2012). Design and testing of a high-temperature superconducting pulsed-power transformer. *IEEE Transactions on Applied Superconductivity*, *22*(2), 5500205-5500205. https://doi.org/10.1109/tasc.2012.2185794.

Li, H., Yan, Z., Zhang, C., Wang, Y., Gao, M., & Zou, G. (2016a). experimental study of inductive pulsed power supply based on multiple HTSPPT modules. *IEEE Transactions on Plasma Science*, *44*(6), 950-956. https://doi.org/10.1109/tps.2016.2558663.

Li, H., Zhang, C., Wang, T., Gao, M., Li, Z., & Zou, G. (2016b). A modified circuit topology for inductive pulsed power supply based on HTSPPTs. *Cryogenics*, *79*, 38-44. https://doi.org/10.1016/j.cryogenics.2016.07.013.

Li, H., Zhang, Y., Zhang, C., Gao, M., An, Y., & Zhang, T. (2018b). A repetitive inductive pulsed power supply circuit topology based on HTSPPT. *IEEE Transactions on Plasma Science*, *46*(1), 134-139. https://doi.org/10.1109/tps.2017.2776564.

Liang, X., Li, H., Zhang, C., Zhang, Y., An, Y., Li, Z., & Zuo, X. (2020). an improved repetitive inductive pulsed power supply circuit with ICCOS technique. *IEEE Transactions on Plasma Science*, *48*(4), 1082-1087.

Liebfried, O. (2017). Review of inductive pulsed power generators for railguns. *IEEE Transactions on Plasma Science*, *45*(7), 1108-1114. https://doi.org/10.1109/tps.2017.2686648.

Lindner, I., Long, J., Girogi, D., Navapanich, T., & Zucker, O. (1986). A meatgrinder circuit for energizing resistive and varying inductiye loads (EM guns). *IEEE Transactions on Magnetics, 22*(6), 1591-1596.

Liu, X., & Yu, X. (2017). The meat grinder with CPFU: a novel circuit for inductive pulsed power supplies. *IEEE Transactions on Plasma Science*, *45*(9), 2546-2551. https://doi.org/10.1109/tps.2017.2739420.

Lu, F. (2020). Research on energy recovery of inductive pulsed power supplies based on SMES. In *2020 IEEE International Conference on Applied Superconductivity and Electromagnetic Devices* (pp. 1-2). IEEE. Tianjin, China. https://doi.org/10.1109/asemd49065.2020.9276234.

Lu, F., Dou, Z., Fan, J., Guo, L., & Jin, N. (2021b). Preliminary analysis and simulation of a 20-Hz repetitive superconducting pulsed power supply. *IEEE Transactions on Plasma Science*, *49*(10), 3154-3161. https://doi.org/10.1109/tps.2021.3114201.

Lu, F., Jin, N., Guo, L., & Fan, J. (2021a). Research on energy recovery of superconducting pulsed power supply. *IEEE Transactions on Applied Superconductivity*, *31*(8), 1-5. https://doi.org/10.1109/tasc.2021.3091089.

Lu, F., Jin, N., Guo, L., Wang, Y., & Yan, Z. (2020). A novel inductive pulsed power supply consisting of a three-winding pulse transformer with parallel switching scheme. *IEEE Transactions on Plasma Science*, *48*(7), 2538-2543. https://doi.org/10.1109/tps.2020.2997682.

Ma, S., Yu, X., & Li, Z. (2015). Determining key parameters for the STRETCH meat grinder circuit. *IEEE Transactions on Plasma Science*, *43*(5), 1485-1490. https://doi.org/10.1109/tps.2015.2413055.

Ma, S., Yu, X., & Li, Z. (2017). XRAM pulse current generator with magnetic flux compression effect. *IEEE Transactions on Plasma Science*, *45*(7), 1190-1195. https://doi.org/10.1109/tps.2017.2701001.

Mcnab, I.R. (2001). Developments in pulsed power technology. In *IEEE Transactions on Magnetics, 37*(1), 375-378.

Pokryvailo, A., Maron, V., & Melnik, D. (1999). Review of opening switches for long-charge fieldable inductive storage systems. In *Digest of Technical Papers. 12th IEEE International Pulsed Power Conference* (Vol. 2, pp. 1341-1344). IEEE. Monterey, CA, USA, https://doi.org/10.1109/ppc.1999.823775.

Schoenbach, K.H., Kristiansen, M., & Schaefer, G. (1984). A review of opening switch technology for inductive energy storage. *Proceedings of the IEEE, 72*(8), 1019-1040. https://doi.org/10.1109/proc.1984.12969.

Sitzman, A., Surls, D., & Mallick, J. (2007). Design, construction, and testing of an inductive pulsed-power supply for a small railgun. *IEEE Transactions on Magnetics*, *43*(1), 270-274. https://doi.org/10.1109/tmag.2006.887685.

Sitzman, A., Suurls, D., & Mallick, J. (2005). *Stretch meatgrinder: A novel circuit topology for reducing opening switch voltage stress*. In *2005 IEEE Pulsed Power Conference* (pp. 493-496). IEEE. Monterey, CA, USA. https://doi.org/10.1109/ppc.2005.300703.

Stoica, V., Dobrin, I., Apostol, S., & Nedelcu, A. (2016). HTS superconducting coils for applications in electrical engineering. *4th International Conference Physics of Materials*, *78*(2), 273-284.

Sun, H., Yu, X., Li, B., Zhu, P., Li, Z., & He, H. (2020). Meat grinder with ACC circuit: a novel circuit for inductive pulsed power supplies. *IEEE Transactions on Plasma Science*, *48*(2), 566-570.

Yu, X., & Chu, X. (2013). STRETCH meat grinder with ICCOS. *IEEE Transactions on Plasma Science*, *41*(5), 1346-1351. https://doi.org/10.1109/tps.2013.2247065.

Yu, X., & Liu, X. (2017). Review of the meat grinder circuits for railguns. *IEEE Transactions on Plasma Science*, *45*(7), 1086-1094. https://doi.org/10.1109/tps.2017.2705164.

Yu, X., Ban, R., Liu, X., & Li, Z. (2017). The meat grinder with SECT circuit. *IEEE Transactions on Plasma Science*, *45*(7), 1448-1452. https://doi.org/10.1109/tps.2017.2705663.

Zhao, B., Li, H., Wang, L., Liu, J., & Liu, X. (2020). A new modular XRAM-like inductive high-current pulse generator circuit topology. *IEEE Access*, *8*, 210158-210166. https://doi.org/10.1109/access.2020.3038451.